Research Article Vol. 30, No. 8 / 11 Apr 2022 / Optics Express 13197
Optics EXPRESS

Characterizing aircraft wake vortex position and strength using LiDAR measurements processed with artificial neural networks

NIKLAS WARTHA,* ANTON STEPHAN, FRANK HOLZÄPFEL, AND GRIGORY ROTSHTEYN

Institut für Physik der Atmosphäre, Deutsches Zentrum für Luft- und Raumfahrt, 82234 Oberpfaffenhofen, Germany
*Niklas.Wartha@dlr.de

Abstract: The position and strength of wake vortices captured by LiDAR (Light Detection and Ranging) instruments are usually determined by conventional approaches such as the Radial Velocity (RV) method. Promising wake vortex detection results of LiDAR measurements using machine learning and operational drawbacks of the comparatively slow traditional processing methods motivate exploring the suitability of Artificial Neural Networks (ANNs) for quantitatively estimating the position and strength of aircraft wake vortices. The ANNs are trained by a unique data set of wake vortices generated by aircraft during final approach, which are labeled using the RV method. First comparisons reveal the potential of custom Convolutional Neural Networks in comparison to readily available resources as well as traditional LiDAR processing algorithms.

1. Introduction

Landing aircraft are again and again exposed to wake vortices that have been generated by preceding aircraft [1]. The wake of an aircraft rolls up to a trailing counter-rotating vortex pair, which in high-lift configuration is at first predominantly made up of wing tip and flap tip vortices [2]. As a consequence, follower aircraft may experience induced rolling moments, a loss in altitude and climb rate, or even structural stresses [3,4], depending on the intrusion path through the trailing wake. The severity of a wake vortex encounter (WVE) is related to the weight of the involved aircraft, its wingspan with respect to the vortex pair separation, and the circulation strength of the vortices [5]. WVEs should always be avoided, especially during the approach and landing phase where glide paths of aircraft align and ground proximity, as well as low flight speeds, limit pilot reactions [6,7]. Awareness of WVE risks caused the ICAO to introduce static aircraft separations after the launch of the B747, which are limiting airport capacities and in numerous studies have been flagged as overly conservative [8]. Although with the ongoing COVID-19 pandemic the air travel sector is facing uncertain times, we refer to the 2018 Eurocontrol forecast stating that even under the worst economic scenario, there would be about 1.5 million unaccommodated flights by 2040 [9], indicating a need for higher aircraft throughput at airports.

The re-categorization program by Eurocontrol and the FAA, termed RECAT, foresees three stages how aircraft separations could be optimized [10]: stage one introduces six new aircraft categories considering the strength of the generated wake vortices and the vulnerability of follower aircraft, stage two features pairwise static separations between aircraft types employing the same principles, and stage three takes into account atmospheric effects on wake vortex behavior, delivering dynamic separations which are adjusted according to the prevailing weather conditions. While stage one is operational at several airports today, stage two shall enter operations at London

#454525 https://doi.org/10.1364/OE.454525
Journal © 2022 Received 16 Feb 2022; revised 25 Mar 2022; accepted 27 Mar 2022; published 5 Apr 2022

Optics EXPRESS

Heathrow airport in 2022. The introduction of stage three would greatly benefit from real-time knowledge of wake vortex position and circulation strength, in order to monitor the predicted wake vortex behavior and the related WVE risks. Proposed Wake Vortex Advisory Systems (WVASs) typically rely on fast-time wake vortex prediction models, like for instance the Probabilistic Two-Phase Wake Vortex Decay Model (P2P) [11], to predict the position and strength of wake vortices. Light Detection and Ranging (LiDAR) instruments with rapid processing algorithms are considered most helpful to monitor the model predictions as a fast-time safety net [12]. Traditionally, LiDAR wake vortex data are processed using algorithms that lack one or more of the following properties: universal applicability to all LiDAR types, complete automation (which is demanding especially in highly turbulent scenarios due to noise, disturbances and environmental vortical structures), fast-time capability, and definitely documented accuracy.

In recent years, machine learning (ML) has also been introduced as a possibility to detect aircraft wake vortices, that is to find out whether or not a LiDAR scan contains wake vortices while also delivering a rough location estimation inherent to the bounding box approach of the algorithm employed. Auspicious results in a qualitative wake vortex search (detecting wake vortices but not quantifying their parameters) within LiDAR scans [13–15] suggest to also use ML for further tasks in this field, in particular Artificial Neural Networks (ANNs). The current paper demonstrates how to take ANNs in this area a leap forward, by fully characterizing the aircraft wake vortices, i.e. quantitatively determining their position and even their circulation. Favorable results can not only allow implementations in support of WVAS, but also provide a new tool for automatic processing of data generated in large wake vortex studies and campaigns conducted for research purposes or as proof of safety of new systems and procedures.

For this work the authors have access to a unique data set of LiDAR measurements originating from a recent campaign conducted at Vienna International Airport. The primary focus of that campaign was to study the effectiveness of so-called plate lines for mitigating the strength of wake vortices in ground proximity (for more insight see [16]). Hence two separate data sets exist: measurements with plate lines erected and measurements with plate lines secured at the ground. In [16] it is found that plate lines may reduce median vortex lifetimes with increasing aircraft size from 22% for the A320 to 37% for the B777. Thus it is also of this paper's interest to determine the influence of plate lines on the characterization of wake vortices. Note that the current effort is highly focused on the measurements from Vienna International Airport. It is a matter of future investigations to enable similar performance on comparable data sets. Nonetheless, we want to highlight that this data set contains some diversity. Five LiDAR measurement locations with different scan geometries, a wide diversity of wake vortex generators (different aircraft types) and prevailing weather conditions spanning different seasons of the year are included. Furthermore, the usage of plate lines has quite a pronounced effect on wake vortex structures.

To learn about the suitability of ANNs for the outlined tasks, this paper considers the following undertakings: generation of artificial LiDAR scan data for the initial development of ANN architectures, normalization of measurement data, development of suitable data pre-processing methods, and comparison and contrasting of common ANN types with regard to their characterization performance and processing time. A precursor version of this paper has been presented at the AIAA Aviation Forum 2021 [17].

2. Background

Before diving into how the ANN architectures were developed and giving a detailed look at the data used to train the ANNs, the following sections provide the reader with context on why the approach and landing phase is of concern in the context of WVEs, gives a thorough look at the state of the art LiDAR processing algorithms, and outlines how previous efforts in using ML for wake vortex detection in LiDAR scans inspired the current effort.

Optics EXPRESS

2.1. Wake vortex behavior near the ground

When approaching the ground, the so-called ground effect sets in. First the wake vortices follow diverging, hyperbolic trajectories starting at an altitude of approximately 1.5 initial vortex separations b_0 above the ground [18]. Below the altitude of about one wingspan, the pair induces vorticity of the opposite sign at the ground surface, creating a boundary layer [19]. Secondary vortices (SV) detach from this boundary layer once the adverse pressure gradient in this boundary layer is strong enough [19]. These SV cause the rebound of the primary wake vortices via induced upward velocities and trigger accelerated wake vortex decay due to the interaction with the primary vortices [20].

When a crosswind is present, an additional boundary layer comes into play, introducing asymmetric vortex decay and transport characteristics as sketched in Fig. 1 (Ref. [7,21,22]). The crosswind vorticity supports the formation of the downwind secondary vortex, but attenuates the upwind secondary vortex. As a consequence, the primary vortex pair tilts and the downwind primary vortex decays more swiftly. In the worst case, at weak crosswinds the more persistent upwind primary vortex may stall over the runway. In contrast, with higher crosswind speeds the downwind primary vortex may move towards a closely-spaced parallel runway [1]. The latter risk is considered by a 2500 ft separation of parallel runways for independent operation [23].

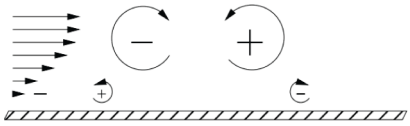

Fig. 1. Vortices in ground proximity with crosswind. Large and small circular arrows represent primary and secondary vortices, respectively (taken from [22], p.1253).

With the touchdown of an aircraft, there is a dramatic lift reduction and its bound vortex vanishes [24]. Inside the vortex cores pressure differences induce axial flow, and outside the cores SV wrap around the primary vortices, mitigating the latter [25,26]. These touchdown phenomena are commonly termed end effects. Obstacles on the ground can also trigger similar effects and may therefore be used to mitigate wake vortex hazards [22]. One optimized variant of such obstacles are the previously mentioned plate lines – a series of upright plates – deployed at the Vienna campaign. Plate lines have been investigated with flow visualization in a towing tank, followed by quantitative particle image velocimetry experiments that already at that stage indicated an enormous capability for accelerating vortex decay [27]. First computational studies using large eddy simulations confirmed the observed and substantiated the understanding of the mechanism involved in the obstacle-vortex interaction visualized in Fig. 2 (Ref. [27]): in the vicinity of the obstacle distinctive SV are formed which approach the original primary vortex. In an Omega-shape, the SV tangle around the primary vortex, leading to the SV's motion in the longitudinal direction of the primary. The two vortices – primary and secondary – circulate in an opposing sense, causing them to attenuate one another and ultimately lead to the premature decay of the primary vortex.

Consideration of practicality, cost and requirements for the installation in an airport environment led to numerous design iterations, with the current plates promising the best compromise. These have dimensions of 4.5 m height and 9 m length and are designed to be separated 20 m from one another [16]. The analysis of over 1000 wake vortex evolutions measured at Vienna airport indicates that the plate lines reduce the lifetimes of the vortices in a safety corridor along the final approach by 22% to 37% depending on the aircraft type. This corresponds to a reduction of vortex circulation by about 50% for the most relevant ICAO separation (Medium behind Heavy) [16].

Optics EXPRESS

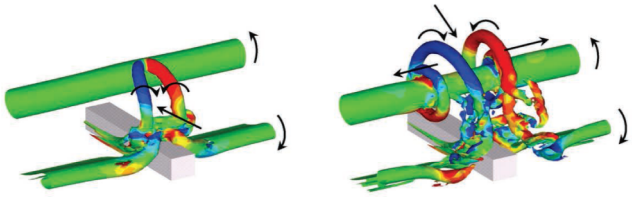

Fig. 2. Secondary vortices emerge and wrap around the primary vortex, propagate along the primary vortex, and lead to its accelerated decay (taken from [27], p.121).

2.2. State of the art LiDAR processing algorithms

Performance scores about the effectiveness of the plate lines in the foregoing section were facilitated by the Radial Velocity (RV) method [28,29] – a cumbersome undertaking as the process is not fully automated. The method considered to be state of the art for LiDAR types with a wavelength of 2 μm used to be the Velocity Envelope (VE) method [30,31]. Its vortex center localization accuracy is determined to be 4.5 m in the vertical direction and 6.5 m in the horizontal direction [32], and the accuracy of circulation strength is quoted with a root mean square error (RMSE) of 13 m^2/s (Ref. [32]). It allows swift evaluation and there are also automated versions available [33].

However, recent LiDAR instruments, such as the micro Pulsed Coherent Doppler LiDAR (PCDL) used during the Vienna measurement campaign, make use of shorter wavelengths of 1.54 μm with weaker Carrier-to-Noise Ratios (CNRs) [29]. The micro-PCDLs called for a new processing approach – the aforementioned RV method [28,29]. Assuming a conservative CNR of −10 dB, the RMSEs of range, elevation angle, and circulation for low turbulence situations (estimates with real LiDAR data and of turbulent scenarios are still pending) are estimated to be 1.8 m, 0.21°, and 10.3 m^2/s, respectively [28]. However, the RV method requires manual input and measurements with a relatively high CNR. Thus, for the complete evaluation of the large wake vortex data base collected at Vienna airport, future comprehensive campaigns or for monitoring purposes with a WVAS, the development of an algorithm facilitating the automated fast-time position and strength characterization of LiDAR wake vortex scans is highly desirable.

2.3. Open research questions and proposed approach

The direction of this work was partly stimulated by previous publications in the field of wake vortex detection with ML and LiDAR measurements. Several ML types have been employed before to detect aircraft vortices in LiDAR scans, for instance Support Vector Machines (SVMs) and ANNs. These studies considered classification of wake vortices i.e. does a LiDAR scan comprise a wake vortex or not (including rough location estimations), with the ANNs delivering an accuracy of up to 94% [13] and the SVMs an accuracy of 70% [34]. The significantly higher accuracy of the ANNs may be tracked back to their ability to recognize unphysical patterns and to automatically determine what to look for [35], compared to SVMs which are often not capable of recognizing complex flow patterns, similar to linear regression. Neither linear regression nor SVMs can be considered applicable for the complex non-linear wake flows developing behind aircraft.

The ANNs developed in [13] are 'You Only Look Once' (YOLO) ANNs [36], a widely adopted pre-defined ANN architecture based on image processing convolutional layers, claiming to be applicable to a variety of image processing problems. However, the YOLO algorithm is a bounding box approach, which refers to its capability to highlight (using a rectangle) the object looked for – in this case the vortex. For regression ANNs, allowing a quantitative analysis, such approach is not desirable, as bounding boxes cannot localize objects with a high accuracy [37].

Optics EXPRESS

On top of this, the nature of capturing objects with boxes is of little use to predict parameters such as the strength of a vortex [38]. Other ANNs used for the classification of wake vortices are either also bounding box approaches [15] or obtain reduced accuracies [14].

This work takes the previous efforts as an inspiration to fully characterize aircraft wake vortices, thus quantitatively determining the position and even the strength (circulation) of the vortices in LiDAR scans, employing custom (not pre-defined) ANNs. The investigated architectures are kept straightforward to build an understanding for the influences of different ANN hyperparameter settings (hyperparameters are all parameters of an ANN that are not trainable) and keep the architectures within reasonable training times on our hardware (Intel Core i7-5600U central processing unit at 2.60 GHz). For each vortex parameter the ANNs output a scalar. Hence, when combining the two positional scalars, the two-dimensional exact position of the vortex can be determined, in the image processing context referred to as key-point detection. Key-point detection is a widely applied ANN method which has received attention in the scene of human pose estimation [37,39] and facial feature detection [40,41]. The benefit of key-point detectors is that, without major restructuring their ANN architecture can also be used for outputting parameters unrelated to the location of objects, such as the circulation strength in the case of this work.

Questions arise when researching previous efforts. In this study we address the following questions.

- Are ANNs also suitable means to quantitatively characterize the position and strength of aircraft wake vortices in LiDAR measurements?
- Do custom ANNs tuned for the task at hand have potential?
- Which fundamental ANN type is preferable?
- What are physical and geometric influences that impact the characterization from the ANNs?
- How can we physically interpret the different ANN components (like filters and layers) in our fluid dynamics application? (Explainability)
- How close do we get to the accuracy of the algorithm used for labeling (RV method)?
- How much faster are ANNs compared to state of the art algorithms (RV method)?

To answer these questions, two custom ANN types are explored: Multilayer Perceptrons (MLPs) allowing fast and efficient pre-processing of the LiDAR data, and the popular image processing Convolutional Neural Networks (CNNs) to obtain higher accuracies, as they frequently win the renowned ImageNet challenge [42]. Additionally, a modified version of the popular pre-defined VGG-16 ANN [43], an often pre-trained ANN, is employed in order to investigate readily available ML resources. Each of these are implemented using the Python module Keras [44]. In a first step we aim to compare the two custom ANNs, in order to confirm that also for our data, CNNs are superior to MLPs. In a second step, the better performing custom ANN is tested against a modified version of the pre-defined and pre-trained VGG-16 ANN to investigate the potential of custom ANN architectures.

3. LiDAR data

The LiDAR measurements used in the current study were recorded at Vienna International Airport during a period from May to November 2019. This data set is the primary focus of the current effort. Figure 3 provides an aerial view of the threshold of runway 16 (seen at the bottom of the figure) with the five LiDAR measurement positions L1 - L5, as well as the two plate lines

Optics EXPRESS

(indicated by red dashes). Three Leosphere Windcube 200S (1.543-µm) micro-PCDLs were operated alternatingly in the five LiDAR positions, hence one overflight usually yields three vortex evolution records. Each of the LiDAR instruments was scanning in a vertical window oriented perpendicular to the runway employing measurement range R spectra from 80 to 530 m. The elevation angle φ spectra and number of beam Lines of Sight (LOS) are listed in Table 1 where the elevation angle step of 0.2° is fixed.

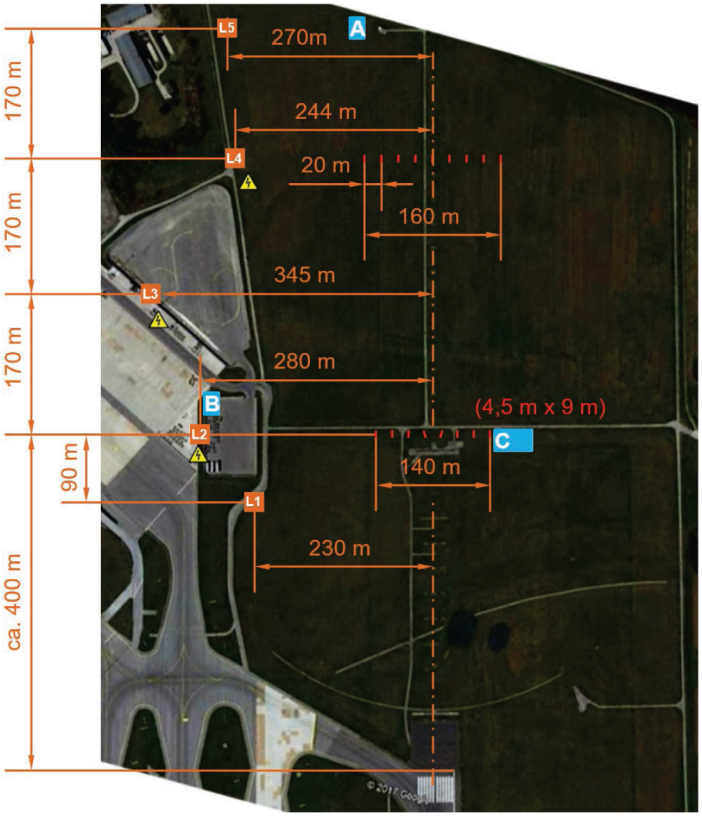

Fig. 3. Campaign set-up (red dashes = plates) (taken from [16], p.5).

Table 1. Scanning parameters in the five LiDAR measurement planes.

LiDAR position	φ range (°)	LOS beams
L1	0 - 25	125
L2	0 - 20	100
L3	0 - 18	90
L4	1 - 28	135
L5	0 - 29	145

LiDAR instruments conduct Range Height Indicator measurements that result in scans of the form sketched in Fig. 4(a). Black dots represent a radial velocity measurement from the LiDAR's perspective, giving the LOS velocity of aerosols at that location through inspecting the Doppler frequency shift between an emitted and backscattered beam [45]. In the Cartesian coordinate system the measurement grid is not equally spaced as shown with Fig. 4(b).

Optics EXPRESS

Obtaining RHI scans for wake vortex detection gives the scenario illustrated in Fig. 5, with the vortex origins (given subscript V) of the clockwise (CW) and counterclockwise (CCW) vortices highlighted. The figure shows the aircraft coming out of the page, with the LiDAR scan capturing a two-dimensional cross section of the wake behind an aircraft. Due to the finite scanning speed the acquisition of a scan is not instantaneous, however the resulting time difference is considered negligible for the purpose of this work. It is also assumed that the two vortices (CW and CCW) share a plane at the same azimuth angle, given that only overflights with low crosswinds and hence minimal aircraft yaws are considered in this analysis.

In total, this paper analyzes 491 vortex pair evolutions, of which 5 are generated by Super, 124 by Heavy, and 362 by Medium ICAO weight class aircraft, each consisting of around 20 associated RHI scans per instrument. Approximate initial vortex circulation strengths for each aircraft class are 650 - 750 m^2/s for Super, 300 - 550 m^2/s for Heavy, and 200 - 350 m^2/s for Medium aircraft. About 41% of the overflight measurements were conducted with the previously mentioned plate lines ('plates up'), whereas the remaining 59% of the LiDAR scans had no flow influence from the plates ('plates down').

4. Artificial neural network architecture development

Before the training of the ANNs with the LiDAR data, the architectures of the ANNs must be engineered. As mentioned before, this paper develops custom MLPs and CNNs, while also comparing performances to an adapted version of the well known VGG-16 ANNs. Custom ANNs are typically developed in hyperparameter studies, which implies that a large number of ANNs are trained and validated using specific metrics. These ANNs differ by altering certain pre-defined 'settings' within the ANN architecture. In this study we aimed for reasonable training times on our hardware, consequently we chose to focus our efforts on identifying hyperparameter tuning trends, rather than fully optimizing the architectures at this stage. The custom architectures are also limited to a manageable depth for exactly this reason, we can investigate a variety of hyperparameters, rather than only the depth, allowing to assess also their effect on characterizing the position and strength of wake vortices. Future studies shall focus on finding an even better suited ANN architecture for this task. Ultimately, the architecture which delivers the lowest characterization error is selected. Efficient hyperparameter studies reveal favorable ANN architecture settings and parameter trends which are not detectable in the pre-defined ANN architectures. To distinguish between ANN architecture shortcomings and effects reflecting the physical nature of the problem, we employ artificially generated proxy data. Indeed, real LiDAR data feature a number of imperfections that might hamper the identification of trends in hyperparameter studies. These include variations and perturbations from signal noise, atmospheric effects such as turbulence, SV, or erroneous data points in the velocity fields captured by the LiDAR instruments. The data set of artificially generated LiDAR scans is used for an unbiased hyperparameter tuning and ANN architecture development, which consists of ideal vortex profiles.

4.1. Artificial proxy data used for efficient hyperparameter tuning

The synthetic data set has the goal of providing clean LiDAR scans that incorporate the counter-rotating primary wake vortex pair (CW and CCW), without turbulence and other atmospheric effects. This artificial proxy data set solely considers vortex models and disregards atmospheric phenomena. Furthermore, the proxy LiDAR scans do not simulate the physical resolution and filtering effects of a LiDAR. This way we efficiently develop ANN hyperparameter settings. Note that the actual training of the ANNs employs real measurement data and the previously defined hyperparameter settings. Further architecture optimization is still possible in future works.

For simplicity, only LiDAR position L3 from Vienna airport is modeled. The Lamb-Oseen vortex model [46] is used to initialize the tangential velocity fields of the primary vortices, with r

Optics EXPRESS

denoting the radius from the vortex center, Γ the circulation, and subscript c the vortex core

$$V_\theta = \frac{\Gamma}{2\pi r}\left[1 - e^{-1.2526(r/r_c)^2}\right] \tag{1}$$

In order to simulate vortex transport, the two primary vortices may have different strengths and can be located independently of each other in the simulated measurement region. Vortices measured by LiDAR L3 generally do not surpass an altitude of 100 m, hence also the simulated vortices are initialized only below the 100 m altitude and are limited to their respective sides of the extended runway centerline. Within these defined areas, vortex locations, core radii and circulation strengths are randomized following the parameter ranges summarized in Table 2.

Table 2. Ranges of proxy data parameters for vortex initialization.

Location parameters	Vortex parameters
$0\ \text{m} \le z_V \le 100\ \text{m}$	$1.5\ \text{m} \le r_c \le 5\ \text{m}$
$80\ \text{m} \le y_{V_{CW}} \le 345\ \text{m}$	$100\ \text{m}^2/\text{s} \le \Gamma \le 500\ \text{m}^2/\text{s}$
$345.0\ \text{m} \le y_{V_{CCW}} \le 520.5\ \text{m}$	

The vortex center locations, $z_{V_{CW}}$, $z_{V_{CCW}}$, $y_{V_{CW}}$ and $y_{V_{CCW}}$ (see Fig. 5) are initialized in the Cartesian coordinate system in order to apply the bounds from Table 2. Since real LiDAR scans are in the RHI format (see Fig. 4), also the proxy LiDAR scans must be transformed to the polar coordinate system. For LiDAR position L3, this leads to elevation-range pairs defined in the field $a(j,k)$, where $j \in \{0, 1, \ldots, 150\}$ belongs to $R \in \{80\,\text{m}, 83\,\text{m}, \ldots, 530\,\text{m}\}$ and $k \in \{0, 1, \ldots, 90\}$ belongs to $\varphi \in \{0°, 0.2°, \ldots, 18°\}$.

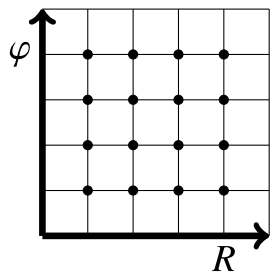

(a) Cartesian measurement grid in the polar coordinate system.

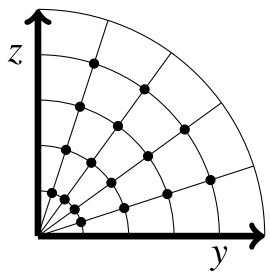

(b) Polar measurement grid in the Cartesian coordinate system.

Fig. 4. Measurement points in a LiDAR scan schematic.

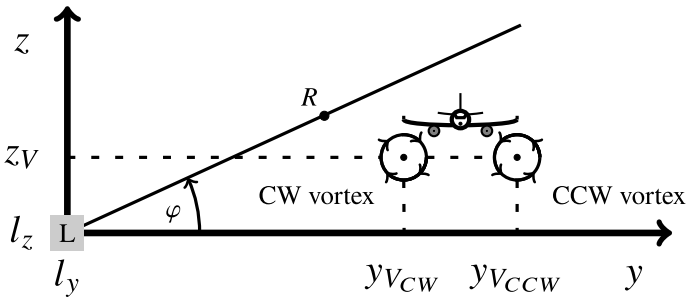

Fig. 5. LiDAR measurement geometry.

Optics EXPRESS

The velocity fields of the counter-rotating vortices are superimposed to obtain a complete proxy LiDAR scan. The following description is given for the CW vortex, deviations to the CCW vortex are also given where appropriate. First, for each prescribed point in $a(j,k)$ the tangential velocity with respect to the vortex core can be found with Eq. (1), where r is equivalent to the Euclidean distance between the respective point and the vortex center. The obtained tangential velocities are then converted to velocity components (v,w) in the Cartesian coordinate system by employing

$$\mathbf{V_{CW}} = \begin{bmatrix} v \\ w \end{bmatrix}_{CW} = \frac{V_\theta}{\sqrt{(z_V - z_k)^2 + (y_V - y_j)^2}} \begin{bmatrix} (y_V - y_j) \\ -(z_V - z_k) \end{bmatrix} \tag{2}$$

For the CCW vortex the signs in the column vector are interchanged. The Cartesian velocity components at each measurement point are utilized to project the velocity onto the radial vector (or LOS) from the LiDAR via Eq. (3), with (l_y, l_z) denoting the location of the LiDAR. This gives the radial velocity V_r with regard to the LiDAR at each point in $a(j,k)$. A sample proxy scan is presented in Fig. 6.

$$V_r = \frac{\mathbf{V} \cdot \left\{ \begin{bmatrix} y_j \\ z_k \end{bmatrix} - \begin{bmatrix} l_y \\ l_z \end{bmatrix} \right\}}{\sqrt{(y_j - l_y)^2 + (z_k - l_z)^2}} \tag{3}$$

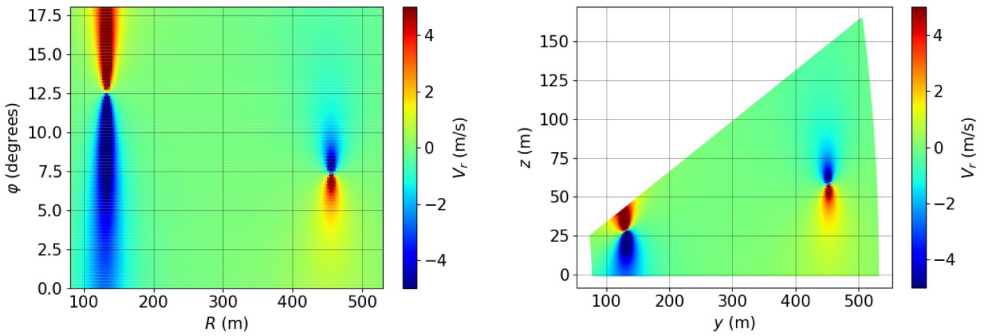

(a) Proxy scan in the polar coordinate system.

(b) Proxy scan in the Cartesian coordinate system.

Fig. 6. Exemplary artificial proxy scan.

4.2. *Specifications of ANNs*

The current section gives an overview of how ANNs operate in general and what components are being used in this work. ANNs are effectively non-linear regressors with the target to dimensionally reduce their input data [47]. In the case of wake vortex LiDAR scans, complex velocity fields must be broken down to a small number of parameters – the two dimensional location and circulation strength of each vortex. In their simplest form ANNs do this with the help of artificial neurons structured in so-called layers, to allow multiple features to be learned simultaneously [48]. Artificial neurons effectively compute a weighted sum of their inputs with the option of thereafter employing an activation function to add non-linearity. ANNs in this work employ the rectified linear unit (ReLu) activation function given its widespread use in regression problems [49] and ability to highlight input regions where the desired pattern is found [50]. Each neuron learns a low-level pattern about the input, which neurons in subsequent layers concatenate to greater common features that the ANNs will be able to recognize in new input

Optics EXPRESS

data. With increasing complexity of the recognized features, the number of features to describe the desired object or parameter eventually reduces to a small number of parameters [47]. To learn high-level features, neurons in deeper layers balance the contribution of features from neurons in the previous layers using weights [48]. In the end, throughout the entire ANN weights are optimized to establish a non-linear relationship between the input and output.

Weights that fulfill this condition are found in a training process called gradient descent, which is employed for supervised ANNs - a type of ANNs that learn the relationship between their input x and output y by comparing the outputs with targets t for N scans. These targets are considered to be the ground truths. In this work, the inputs are the LiDAR scans and the outputs are the parameters to characterize the individual vortices, namely the range R_V and elevation angle φ_V which define each vortex center, and the circulation strength Γ. The targets are derived from the RV method and are of the same format as the outputs. The schematic in Fig. 7 provides an overview of the gradient descent algorithm and demonstrates a loss function $L(w)$, where w represents the weights, as one possible way of comparing the outputs y_N of the ANN and the targets t_N. The herein chosen loss function is the mean squared error (MSE), given its widespread use in ANN regression problems. Once the loss function is computed, the gradient with respect to each weight is established. In the final step of this algorithm all weights are updated in the opposite direction to their respective gradient, at a magnitude dictated by the network training learning rate η. Often an optimizer function is also applied, simplifying the discovery of minima in the weight space. This entire process is repeated for M epochs (or iterations), to allow enough opportunity for weights to adapt. Unless the MSE does not reach its minimum for 30 epochs, training in this work is executed for 100 epochs. An early stopping point allows avoidance of overfitting to the training data.

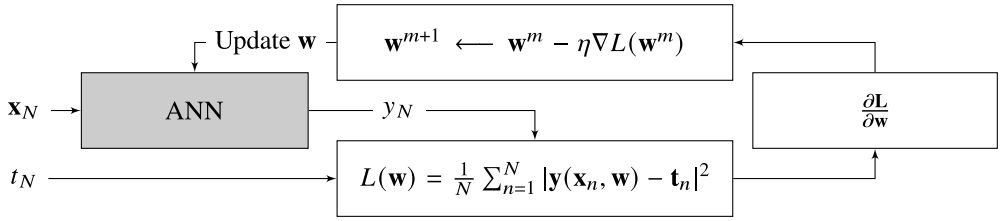

Fig. 7. Schematic of the gradient descent algorithm (inspired by [51], p.5).

Each ANN presented in this paper has been evaluated using at least two independent data sets, a training data set and a validation data set, where the former is typically larger. LiDAR scans of complete vortex evolutions have always been allocated in full either to the training or the validation data set in order to avoid any previous knowledge resulting from similar vortex constellations. To finalize the general specifications of the ANNs we turn our attention to normalization. Typically ANNs can deal better with input data that has a low variance [49]. To facilitate this all LiDAR scans, whether used for training, validation, or future assessment, are normalized such that all measurement points of the complete training data set are taken into account to establish a training data set with a radial velocity mean of zero and a standard deviation of one.

Above ANNs were described with artificial neurons which to a large extent operate individually within each layer. However, a wide range of other ANN layer types exist, also including layers that use data transfer within themselves. The following sections briefly describe the layer types employed in this work, where appropriate the formula for calculating the number of trainable parameters in a layer is also given. The number of trainable parameters within an ANN can drastically influence the training and processing speeds of an ANN.

Optics EXPRESS

4.2.1. Dense layer

This layer is the classic building block of an ANN. Each neuron is connected to all neurons in the previous and following layer, but within the layer itself neurons are not interconnected [52]. The input to a dense layer consists of a one-dimensional array of radial velocities (for the input layer the product of a scan's height and width is used). Typically dense layers are not known for context understanding in image processing activities, however to enable some spatial context understanding the number of neurons in the first layer can be less than the number of inputs, thus the neurons consider several radial velocities at once. Dense layers are also crucial in regression ANNs where other layer types are employed, they are required as a final output layer to reduce the parameter space to a size of unity [53]. The number of trainable parameters P_d of such a layer l is computed using Eq. (4), where OS is the output shape (the number of neurons in the layer) and IS is the input shape (the number of individual data points arriving to the layer per scan). The parameters are made up of the weights and bias (giving the +1) of each neuron in the layer.

$$P_d^l = OS^l \left(IS^l + 1\right) \tag{4}$$

4.2.2. Convolutional layer

Within convolutional layers the artificial neurons are employed in a slightly different manner. The neurons are arranged in matrices called filters, which use the convolution operation to create activation maps that indicate where and at what magnitude patterns are found [49]. Through this, velocity patterns in the LiDAR scans can be trained and reused for newly incoming data [54]. These filters can also be seen as receptive fields that scan across the input in search for patterns it has learned. These patterns will be detected no matter what their position within the input data is – a phenomenon called shift invariance. The input to a convolutional layer is three-dimensional comprised of the width and height of a LiDAR scan grid, as well as the number of channels (or depth) of the data which is then transformed into the number of filters. Padding and stride are additional means to influence the output from a convolutional layer [49]. Padding attaches borders to the output such that the scan size remains constant, whereas stride refers to how many pixels a receptive field is shifted within a scan between each convolution computation. By using the same filters across the entire scan, less weight parameters are required in comparison to dense layers. The number of trainable parameters P_c of such layer is calculated using Eq. (5), where OC is the output channel size (the output shape refers to the number of filters in the layer), IC is the input channel size, and $F_h \times F_w$ are the filter height and width, respectively.

$$P_c^l = OC^l \left[(IC^l \times F_h \times F_w) + 1\right] \tag{5}$$

4.2.3. Pooling layer

The purpose of pooling layers is to reduce the number of trainable parameters in order to force high-level features to be learned from low-level ones and thus only regard salient features [52]. Typically pooling layers follow convolutional layers, forming so-called ConvPool blocks, which has the consequence that pooling layers make use of the same data shape as convolutional layers. Max pooling is usually the preferred pooling type [55], as in a receptive field of an activation map only the most salient feature is highlighted. The pooling layer has no trainable parameters.

4.2.4. Flatten layer

This layer type can be seen as a data shape transformation layer. It converts highly dimensional data to one dimension [49]. As described previously, for the output of a regression ANN a final dense layer is necessary, hence a flatten layer must be employed for CNNs. This layer also has no trainable parameters.

Optics EXPRESS

4.3. Hyperparameter tuning

By employing the previously introduced proxy data set the two custom ANN architectures MLP and CNN were developed. Selected hyperparameters were varied within reasonable ranges and the performance of the ANNs was compared to other hyperparameter settings via the mean absolute error (MAE). The hyperparameter settings providing the lowest MAE were selected as the settings of the custom ANN. The following sub-sections specify which hyperparameters were studied for each custom ANN architecture. It has previously been emphasized that the purpose of this paper is to gather an understanding about the suitability of ANNs for the task at hand. Consequently, we limited hyperparameter tuning with the aim to obtain expertise in what 'direction' a hyperparameter should be tuned for improved wake vortex characterization performance. Furthermore, hyperparameter settings which proved to operate well in one ANN type were, where possible, transferred to the other ANN type.

In order to increase the reader's understanding of how we arrived at our custom ANN architectures, the first hyperparameter study is detailed. It assessed whether it is preferable to train one ANN which characterizes all parameters at once, or whether performance would improve with scalar ANNs, where only one parameter is evaluated at a time. It was found that scalar ANNs deliver superior results, this implies the need for six separate ANNs to operate simultaneously, each trained for one of the characterization parameters - $\varphi_{V_{CW}}$, $\varphi_{V_{CCW}}$, $R_{V_{CW}}$, $R_{V_{CCW}}$, Γ_{CW}, Γ_{CCW}. Figure 8 displays the circulation Γ MAE of the CW vortex versus the training epochs. The study for the custom CNN architecture investigates whether performance increases when using more or fewer ConvPool blocks. We see characterization errors can be decreased with an increase in ConvPool blocks. Furthermore, patterns are learned faster - less epochs are needed for a low MAE. Thus, the choice for the custom CNN architecture was to employ 4 ConvPool blocks. It seems plausible that more ConvPool blocks (such as 8 or 16) would decrease the error further, however given that part of this work is to investigate the suitability of such methods for wake vortex characterization on our hardware, architectures of that depth are not further considered herein. The full spectrum of hyperparameter studies resulted in the ANN architectures presented in Fig. 9, further descriptions follow below.

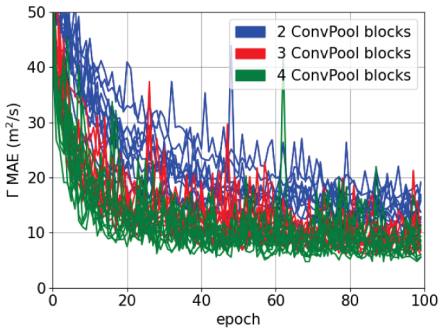

Fig. 8. CNN hyperparameter comparison with validation proxy data & the CW vortex circulation strength to identify a suitable number of ConvPool blocks.

4.3.1. Custom MLP architecture

The custom MLP architecture is illustrated in Fig. 9(a). Modified hyperparameters included the number of dense layers, the number of neurons per layer, the dropout rate, and the optimizer type. The hyperparameter studies elucidated that overfitting to the training data set may be avoided by limiting the number of neurons per layer to 64 and by employing the Adaptive Moment Estimation (ADAM) optimizer [56]. Regularization techniques are often included in ANN architectures to

Optics EXPRESS

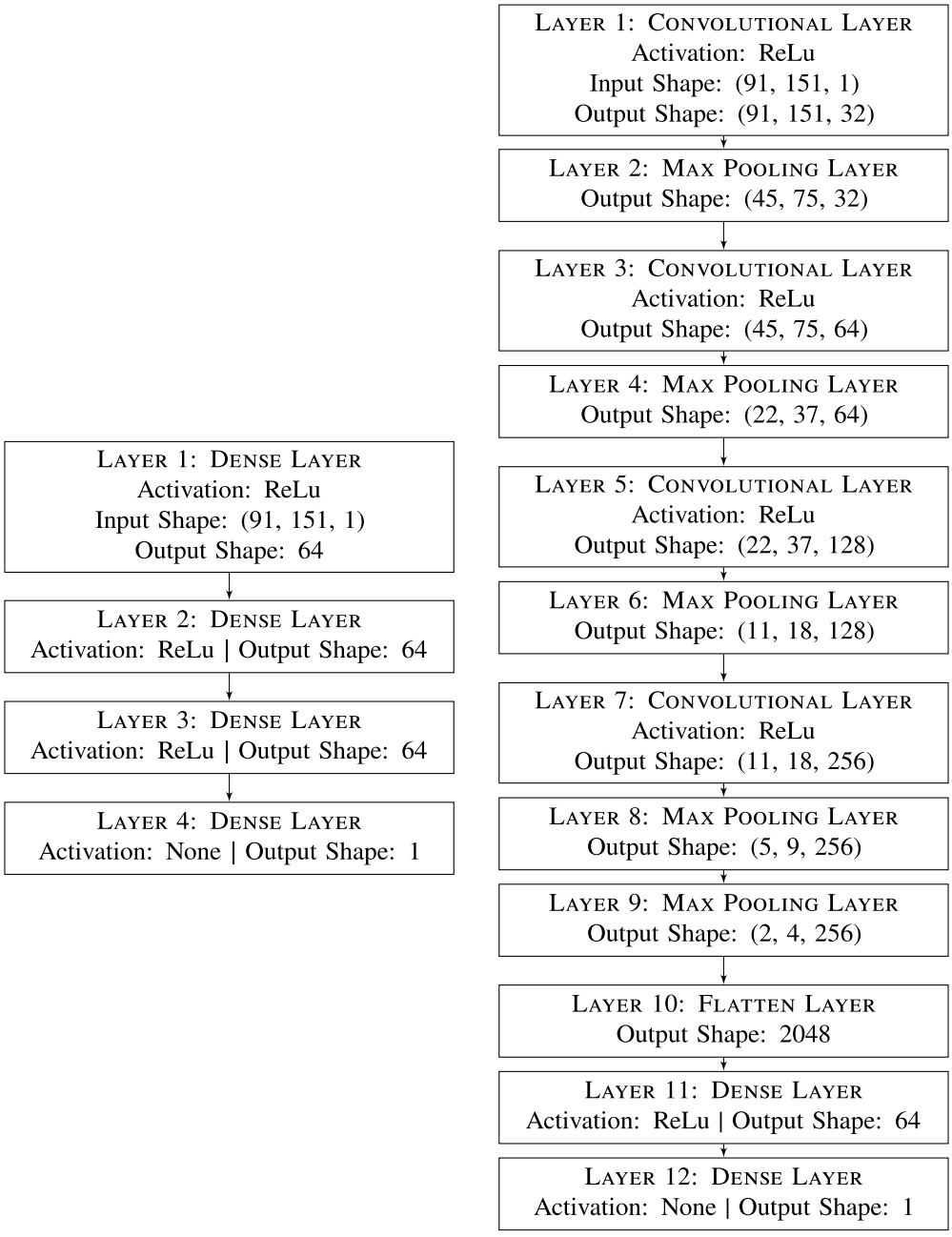

(a) Multilayer Perceptron (MLP) architecture.

(b) Convolutional Neural Network (CNN) architecture.

Fig. 9. Custom scalar regression ANN architectures.

Optics EXPRESS

avoid overfitting. Here regularization techniques are not used as it appeared that they deteriorate the performance of the trained ANNs. Due to their rather inefficient structure, the number of trainable parameters of MLPs is large. LiDAR scans of pixel size 91×151 (number of LOS times range gates) result in 887873 trainable parameters when using Eq. (4) and adding up the results for each of the layers.

4.3.2. Custom CNN architecture

Figure 9(b) shows the custom CNN architecture. One early decision had to be made about whether LiDAR scans would have to undergo transformation from the usual polar to a Cartesian coordinate system. This transformation was only considered for the CNN architecture, given its shift invariance attribute. The concern was that polar coordinate scans could distort and overestimate vortices and hence CNNs would not perform as successful as in translation invariant problems [57]. However, an elementary transformation to the Cartesian coordinate system only led to negligible performance improvements and hence was not considered further in this paper. Hyperparameter settings which were not tuned were given standard values, that is [49]: the filter size of the convolutional layers is 3×3, the padding is such that the scan size does not alter with the convolutional procedure, and the stride is set to unity. Instead, the pooling layers have a filter size of 2×2 and stride of two, reducing the scan size by half with each pooling layer [54]. Modified hyperparameters included the number of ConvPool blocks, the pattern which dictates the number of filters with depth of the ANN, the number of filters in the first layer, and the number of dense layers. Hyperparameter tuning suggested that 32 filters in Layer 1 and subsequently doubling the number of filters with each ConvPool block, in order to counteract the decreasing scan size (due to the pooling layers) and hence store the learned information, deliver the best results. The total number of trainable parameters is 519041 for LiDAR scans of pixel size 91×151 (computed using Eq. (4) and Eq. (5)) - nearly half the number of trainable parameters compared to the MLPs.

4.3.3. Modified pre-trained VGG-16 architecture

The VGG-16 architecture is a pre-defined CNN developed by the Visual Geometry Group (VGG) at the University of Oxford [43]. In this work, small adaptations have to be undertaken to make it suitable for the current application. The majority of layers in the VGG-16 architecture are pre-trained on the exhaustive ImageNet data set to maintain reasonable training times on our hardware. This is a standard operation for transfer learning applications, however it is to be seen whether such different data set also allows seeing patterns in wake vortex LiDAR measurements. Furthermore, the deepest layers of the VGG-16 architecture are adjusted to suit the desired application (a common operation [49]). These are the only layers which will be trained with the data set from Vienna International Airport. We recognize that the ImageNet data set is based on images from a variety of different objects. However, as this is a readily available resource we find it attractive to explore its capabilities for our wake vortex characterization task. The standard VGG-16 settings and architecture are presented in [43]. We adapted this architecture by removing the top three dense layers and replacing them with a flatten layer, followed by a dense layer with 64 neurons, and a further dense layer – the output layer – with a single neuron. Input to the VGG-16 ANN must have three channels, representing RGB images. Since LiDAR measurements are radial velocities with only one value, the go-around is to plant each measurement point three times with the same radial velocity. This adaptation to the input data should not affect the performance of the ANN by much, as the gradients between grid points remain the same. The number of parameters in this network can be found with the usual equations, but in this case only 32897 out of the 14747585 parameters are trainable for LiDAR scans of pixel size 91×151 - an order of magnitude less compared to the custom MLP and CNN architectures. Given the modifications undertaken of the VGG-16 architecture, this effort cannot assess whether custom

Optics EXPRESS

or pre-defined ANN architectures perform superior in general, but only judges the specific ANN set-ups found herein. It is expected that VGG-16 ANNs trained exclusively on wake vortex LiDAR measurements will perform in a superior manner.

5. Pre-processing of LiDAR measurements

Having established the ANN architectures, the focus now shifts from the proxy data set to the LiDAR data from Vienna airport. As previously noted the data from Vienna airport is more complex, as it contains atmospheric phenomena such as turbulence and crosswind. Moreover LOS at a low elevation angle measure points in space which are obstructed by a boundary layer and/or erected plate lines.

5.1. Handling varying numbers of vortices in LiDAR scans

Captured LiDAR scans sometimes contain more or less wake vortices than the counter-rotating pair which the ANNs are built for. A higher number of vortices is typically seen when landing aircraft are staggered closely causing old vortices to remain in the LiDAR measurement window even after the follower aircraft has already passed the measurement plane. Only one wake vortex is found in a LiDAR scan when the other vortex has convected out of the measurement window, which usually occurs towards older vortex age. At Vienna airport the LiDAR instruments were continuously scanning, which also implies that many LiDAR scans without any wake vortex exist. However, since the detections computed by the RV method are adopted as the targets for the ANNs, these 'empty' scans are already disregarded from the data set used for training and validation beforehand. LiDAR scans with more than two wake vortices are handled by being used multiple times. For instance, a LiDAR scan with three vortices will once be treated for the vortex pair and once for the remaining vortex. Managing such cases with only one vortex is facilitated by setting unavailable targets – the targets of the non-present vortex – to zero. Fixing unavailable targets to a pre-defined value is a common approach for missing data in ANNs, yielding the ability to learn that this value is designated for missing data.

5.2. Reducing crosswind effects

To keep the vortex structures as consistent as possible, an approximately constant crosswind is subtracted using a background LiDAR scan, recorded just before the aircraft crossed the measurement plane. These crosswinds should not change significantly over the time delay between the background scan and the LiDAR scan of interest, also because this study only considers worst-case WVE conditions, that is weak winds. The mean radial velocity of each background LOS is subtracted from the vortex scan's associated LOS. This technique for minimizing crosswind effects is also part of the RV processing method.

5.3. Mitigating influences of plates and SV

ANNs make strong use of gradients. Boundary layers generated by the wake vortices at the ground and the detachment of SV as well as the interference of the wake vortices with the plates may cause significant velocity gradients, making the ANN wake vortex characterization more challenging. A method for lowering the influence of such disturbances is to disregard the data collected in their vicinity by setting the corresponding values to zero. An appropriate elevation angle threshold, underneath which measurements are disregarded has been determined as illustrated in Fig. 10.

Neglecting measurements below an altitude of 7 m at the runway centerline ensures that laser beams do not encounter a plate. This cut-off height also clips off substantial parts of the SV detaching from the ground boundary layer while at least the vortex cores even of the smallest

Optics EXPRESS

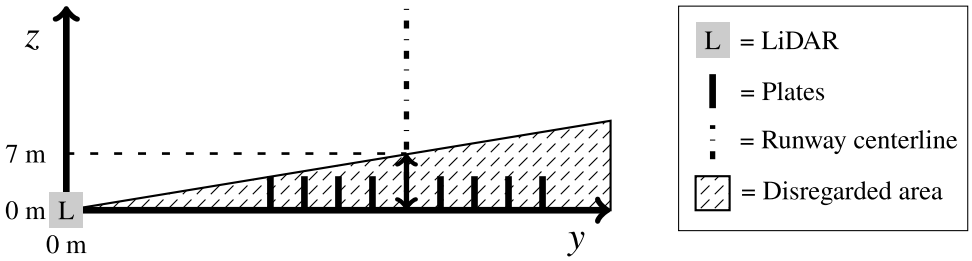

Fig. 10. Schematic of the disregarded LOS area.

considered aircraft type (A320), typically descending down to a minimum height of half of their initial vortex separation $b_0/2$ =13.4 m (Ref. [7]), can still be captured.

5.4. Expanding generalizability of the ANNs

When ANNs are confronted with new data sets, their performance is linked to their ability to generalize - so the question is 'how well can the ANN adapt?' Good generalizability makes ANNs robust for new situations and increases the algorithm's trustworthiness. For this work, our data set is limited to measurements from Vienna International Airport. Consequently, generalization to measurements from set-ups, other than that of the Vienna campaign, is beyond the scope of this work. Nonetheless, for the Vienna campaign generalizability can be introduced by training ANNs with LiDAR scans from all five LiDAR positions at once. A universal measurement grid was developed using nearest-neighbor interpolation. From Table 1 the maximum and minimum elevation angles were chosen to size this grid. LiDAR scans which have a smaller elevation angle spectrum fill the missing measurement points with zeros, bypassing the necessity for spatial scan normalization due to vortex distortions. An exemplary comparison of MLP results obtained with scans only from LiDAR position L2 versus MLP results obtained with scans from all LiDAR positions is given in Table 3. Metrics include the MAE of each vortex parameter and ΔD, which represents the Euclidean distance between the vortex core defined by the RV method and the ANNs. Mean and median ΔD differ due to a low number of significant outliers. Typically large discrepancies between the RV method and ANNs occur when the latter detect a turbulent eddy rather than a wake vortex. Note that MLP results in subsequent sections will differ to these below, as this study did not employ all other pre-processing methods yet.

Table 3. Validation errors comparing MLPs from LiDAR position L2 with 1000 train and 65–100 validate scans and MLPs from all LiDAR positions with 9187/6708 train & 700–1000 validate scans (plates down/up) (gray = lowest error per parameter & plates state).

Plates	Γ MAE (m^2/s)		φ_V MAE (°)		R_V MAE (m)		Mean/median ΔD (m)	
& LiDAR	CW	CCW	CW	CCW	CW	CCW	CW	CCW
Down								
L2	37.77	33.22	1.66	0.91	27.70	35.14	28.59/16.85	36.80/24.04
L1-L5	37.41	33.13	1.84	1.00	27.18	26.76	29.45/18.94	28.29/18.63
Up								
L2	41.52	39.62	1.72	1.07	37.59	40.23	39.53/24.66	41.89/26.33
L1-L5	40.36	42.91	1.56	1.14	31.96	36.39	33.81/22.92	38.31/23.41

Concatenating LiDAR scans from all LiDAR positions significantly increases the size of the data set available for training the ANNs. This directly counters the increase in velocity field variability which is introduced by the different LiDAR positions capturing slightly different

Optics EXPRESS

observation fields and wake phenomena. The universal ANNs have similar characterization capabilities, while also appearing independent from the position of the LiDAR.

6. Results

This section is dedicated to the analysis of the potential of ANNs to characterize the wake vortices and to answer the open questions listed in Section 2.3. It has been found that large deviations of the determined vortex positions typically are related to factors, such as incorrect data labels, which the ANN cannot influence. Thus, cases that might yield misleading rating of the ANN performance are excluded and the validation data are restricted to LiDAR scans with exactly two wake vortices. LiDAR scans with a single vortex typically cause large errors for the missing vortex, because the ANN places the vortex at the origin either earlier or later than the RV method. Similarly, when an additional vortex appears within a LiDAR scan, labeling of the data becomes challenging, as it is often difficult to assign the vortex to the current or previous overflight.

It was also found that training separate ANNs for cases with and without plate lines yields superior performance. Further, splitting the data set also allows an analysis of the plate line effects on the characterization capabilities of ANNs. As will be detailed further in the coming sections, the separate ANN models also allow drawing conclusions on the effect of plate lines on the flow field of the aircraft wake, regardless of which ANN type is analyzed.

6.1. Comparing the custom multilayer perceptrons and convolutional neural networks

Table 4 lists the validation results of the two custom ANNs in terms of the mean absolute error (MAE) and the vortex location error ΔD. The color coding highlights that CNNs outperform MLPs in most categories. In fact, there are only two parameters where this is not the case: the CW R_V and ΔD for the erected plates, where the ΔD error is mainly based on that of R_V.

Table 4. Validation errors comparing MLPs and CNNs with 8925/6520 train and 700–1100 validate scans (plates down/up) (gray = lowest error per parameter and plates state).

Plates	Γ MAE (m^2/s)		φ_V MAE (°)		R_V MAE (m)		Mean/median ΔD (m)	
& ANN	CW	CCW	CW	CCW	CW	CCW	CW	CCW
Down								
CNN	32.24	25.76	1.40	1.00	21.51	20.51	22.70/11.49	21.89/12.39
MLP	44.69	39.43	2.19	1.48	37.62	38.57	29.37/28.42	40.26/33.82
Up								
CNN	33.21	31.08	1.36	0.85	45.88	46.24	46.70/39.50	46.90/31.60
MLP	53.26	51.77	2.03	1.35	39.34	50.96	41.55/28.23	52.25/39.30

In the majority of categories, the CW wake vortex turns out to be harder to characterize than the CCW wake vortex. Three main factors exist that may cause this difference, all of which are related to the usual vortex position in the measurement field: the grid coarseness, the LiDAR focal length and the number of vortex measurements available for the training of the ANNs. We claim that a coarse grid has little impact on the characterization precision of ANNs, as from Fig. 4(b) we know that the CCW vortex is normally placed in the coarser grid region. It should also be noted that CNNs deal with coarse grids in a superior manner. Given this low impact of the grid coarseness, it may be claimed that the LiDAR focal length has a higher significance for the characterization precision. LiDAR instruments need to have their laser focused before usage, on a location where the CNR will be highest. Given that at Vienna airport all LiDAR instruments were set to have a focal length of 500 m, the CNR of measurements near the CCW vortex is usually higher than for the CW vortex. Furthermore, with roughly 20% more CCW vortices than CW vortices, we expect the latter to be characterized with a lower precision in any case.

Optics EXPRESS

From Table 4 it is also evident that wake vortices are more difficult to characterize when they are influenced by plate lines. While the circulation strength is marginally worse with plates, the localization takes a considerable hit. This result is also of importance to the study of plate line effects, as it indicates that the plates effectively perturb the coherency of the wake vortex structure, this way making generalizations for the ANNs more challenging. For illustration purposes, Fig. 11 provides time frames of detections by the custom CNNs and the RV method for an overflight of a B777 without plate lines. It is evident that young vortices that are still coherent, of high circulation strength, and distinct from turbulence, are characterized with a high precision. Hence, the CNNs perform well during the state in which vortices are considered to be the most dangerous to follower aircraft. On the other hand, follower aircraft are unlikely to be closer than 60 s behind a Heavy generator aircraft as they have to obey minimum radar separation and thus the relevant time frames rather start after 60 s of an overflight. Towards later times predictions deteriorate, especially for the CW wake vortex as it is occasionally transported out of the LiDAR's measurement window. At this progressed state of vortex erosion, it is not straightforward to know whether the RV method, which constitutes the CNNs' targets, or the CNNs themselves are more accurate. Moreover, distinguishing the background turbulence from the primary vortex pair is a challenge. However, also when the key-point localization is less accurate, the circulation is correctly predicted as low (see the CW vortex in Fig. 11(f)). Thus, a false alarm would become unlikely when considering both the determined position and strength of a vortex.

6.1.1. Localization

Although a hazardous vortex will ultimately be defined by its location in combination with its circulation strength, the individual analysis is crucial for understanding what aids and what hinders the workings of the ANNs, as well as for comparing the custom MLPs and CNNs. Straight from Table 4 it can be stated that CNNs reduce the R_V MAEs by up to 47% and ΔD by up to 63% by comparison to the MLPs in the plates down case. Absolute elevation angle precisions increase by up to 0.8° with the CNNs. When plotting ΔD against vortex age t for each ANN type in Fig. 12, it is revealed that the custom CNNs provide far fewer high magnitude outliers and generally result in lower errors – especially at a young vortex age. For completeness also the VGG-16 results have been included in the figure.

The distribution of ΔD errors in Fig. 13 delivers further insight into the difference of the localization precision between the two custom ANN types. The clearest trend is manifested for the cases without plates displayed in Fig. 13(a): CNNs are to a great part extremely accurate as indicated by the high count of low ΔD. The errors of MLPs on the other hand are more spread out along the ΔD-axis. With plates less significant differences between the ANN types are observed.

Figure 14 illustrates the median ΔD of the two ANN types on top of exemplary LiDAR scans. The ellipses result from all LiDAR scans in the respective validation data sets, the illustrated LiDAR scans therefore only provide a perspective of the accomplished localization precision. All ANNs can identify vortices with a satisfactory precision.

Operationally critical for aircraft separations is knowledge of the WVE risk for a follower aircraft, exact localization capabilities are not necessarily required. Instead, it is of interest whether a vortex is generally still hovering above the runway, posing a 'potential hazard'. Thus, we define a ±50 m lateral safety corridor (inspired by [16,58]) outside which vortex evolution is irrelevant. On the other hand, vortices of any strength within this corridor are considered a potential hazard to follower aircraft. Several statistical metrics were computed in Table 5, which mostly confirm the preeminence of the localization with CNNs, especially when considering the plates down ANNs. Row 1 compares the localization of the RV method and respective ANN, whether their regions – within or outside the corridor – match. Considerably more vortices are located in the correct region with CNNs, while also being more conservative as less vortices

Optics EXPRESS

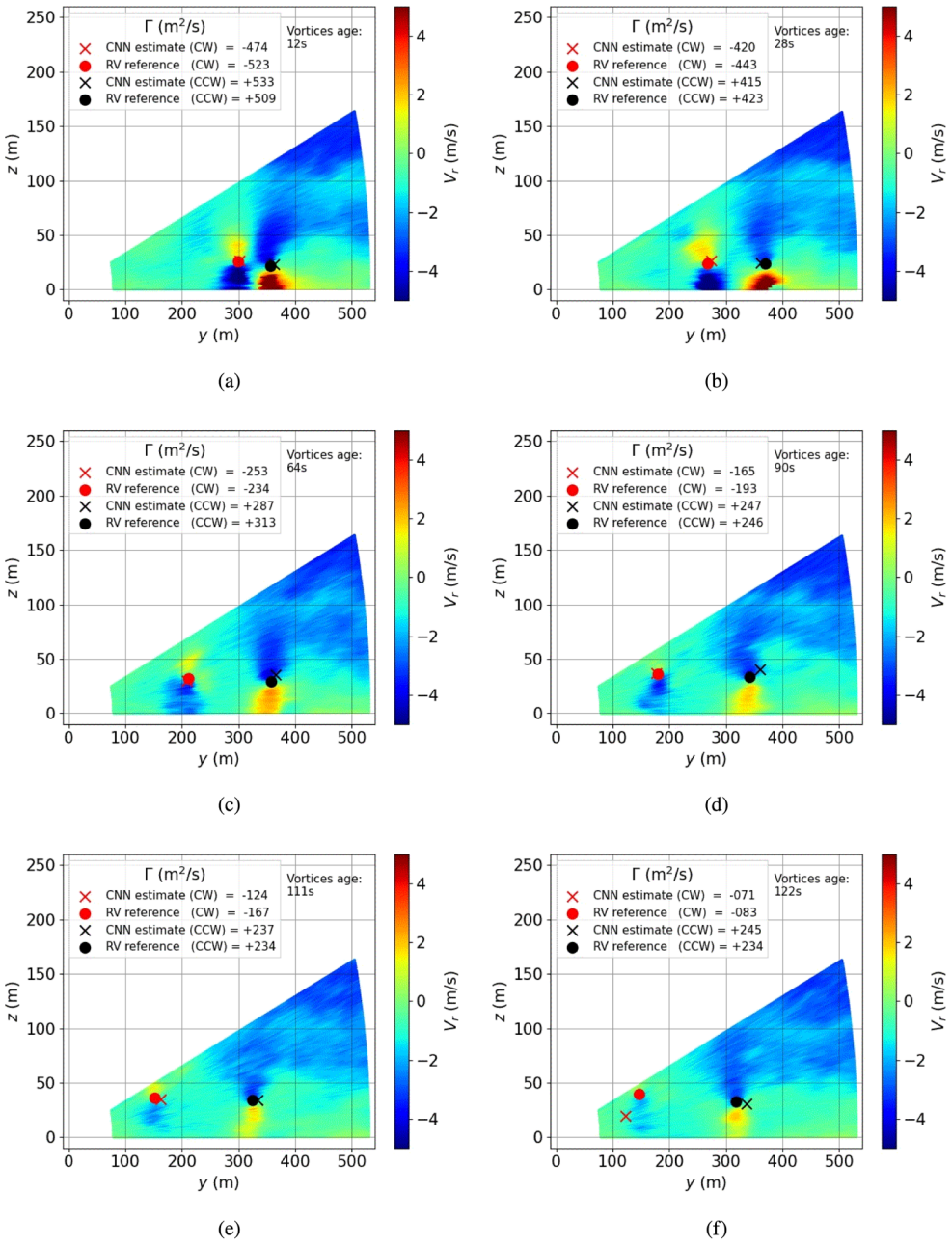

Fig. 11. Time frames with predictions and targets of the custom CNNs of a B777 overflight without plates.

Optics EXPRESS

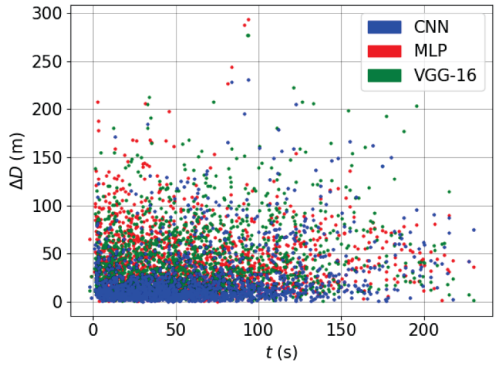

Fig. 12. ΔD dependent on vortex age for different ANN types without plates.

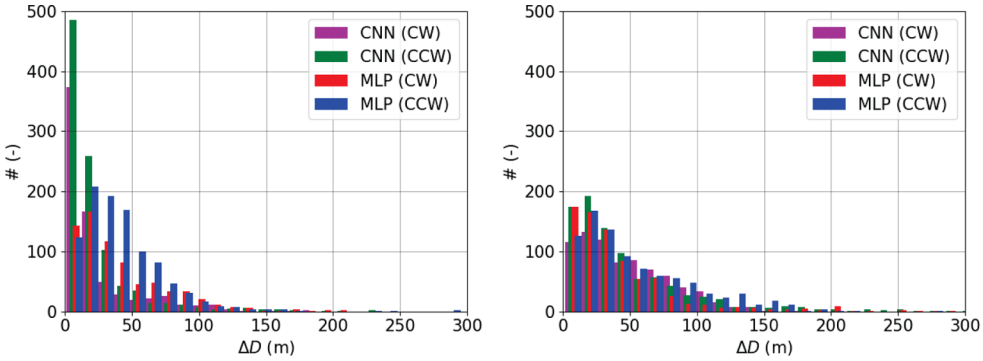

(a) Plates down. (b) Plates up.

Fig. 13. ΔD distributions of the ANNs comparing MLPs & CNNs.

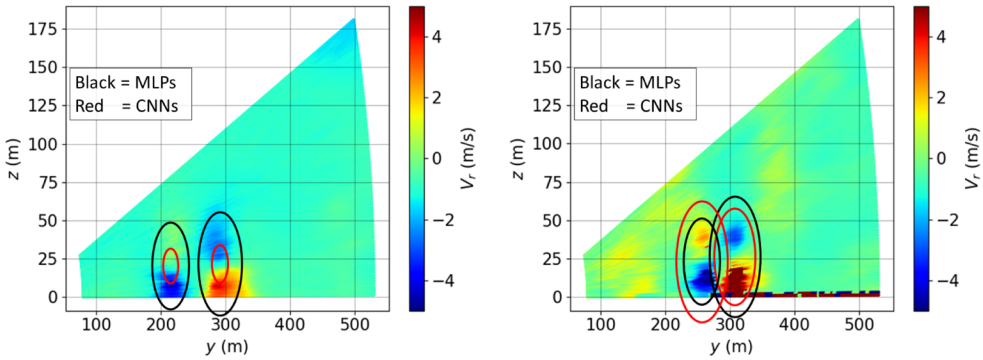

(a) Plates down. (b) Plates up.

Fig. 14. Median ΔD ellipses on exemplary LiDAR scans comparing MLPs & CNNs.

Optics EXPRESS

are labeled as 'no potential hazard', when in reality they are a potential hazard as quantified by the False-Negatives rate ($FNR = FN/(FN + TP)$). The False-Positives rate is defined as $FPR = FP/(FP + TN)$. In general, False-Negatives (FN) are more common than False-Positives (FP). Note that correct vortex allocations are analogously defined using True-Negatives (TN) and True-Positives (TP). Lastly, a superiority of the positive predictive rate ($PPR = TP/(TP + FP)$), the probability of predicting a potential hazard when there actually is one, is obtained with CNNs - it is considered to be one of the most vital metrics.

Table 5. Statistics regarding localizations in a runway corridor (CW and CCW vortices). Positive/negative are vortices within/outside the corridor (gray = superior network per plates state). The RV method is used for comparison.

Localization metric	Plates down		Plates up	
	MLP	CNN	MLP	CNN
ANN and RV method match (%)	67.6	86.0	64.6	66.1
False-Positives rate (%)	19.3	13.4	38.5	26.7
False-Negatives rate (%)	43.2	14.5	33.5	38.5
Positive predictive rate (%)	78.2	88.6	73.3	78.6

Figure 15 shows localization errors ΔD for the CNNs against the vortex age and circulation strength dependent on the RV method while differentiating between aircraft types detected at Vienna airport. Note that the A320neo (A20N) is included in the A320 category, as it features the same maximum landing weight and wingspan as the A320 does. The dark gray area is limited by the 25th and 75th percentiles, whereas the light gray area encloses the 5th and 95th percentiles. The vortex-age-bins have dimensional widths of 30 s and circulation-bins have dimensional widths of 50 m^2/s (with the exception of one circulation-bin which spans 500 m^2/s to 600 m^2/s). Figure 15(a) indicates a trend of decreasing precision of wake vortex localization as the vortices become older. This correlates well with Fig. 15(b), older vortices are weaker and typically less coherent. However, we can see that far less data points exist at older vortex ages, which makes the percentiles less reliable. Figure 15(b) indicates that there is a threshold circulation strength at around 100 m^2/s, below which the CNNs struggle to localize the vortices. This is expected and vortices below a certain strength are not of concern for a follower aircraft - while there is no agreement on an acceptable wake vortex strength that can be taken as a safety boundary in the wake vortex community. Beyond this limit, the CNNs deliver promising localization capabilities for the majority of the LiDAR scans. Note that also the increased number of high ΔD at young vortex age is expected as the vortices typically need a certain time to complete roll up [59], yielding a vortex structure which deviates from the coherent structure that the majority of vortices feature in the data sets.

6.1.2. Circulation

It is argued that shift invariance constitutes the most powerful asset of CNNs and clearly aids the localizations of the wake vortices. In comparison to MLPs, CNNs also characterize the circulation strength with a higher precision, however the improvement is not as drastic as for the localization. Figure 16 compares the circulation values achieved with the ANN types considered in this paper to reference values of the RV method. MLPs overestimate the number of young weak vortices, while the CNNs are in the same order of magnitude as the RV method. Similar to the localization, MLPs are more likely to result in False-Negative estimates of circulation values than CNNs, leading to potentially dangerous situations for follower aircraft. A closer look also reveals that the data cloud is less spread out for CNNs, hinting lower circulation errors. Figure 16(c) showing the circulation estimates of the VGG-16 ANNs is provided for completeness.

Optics EXPRESS

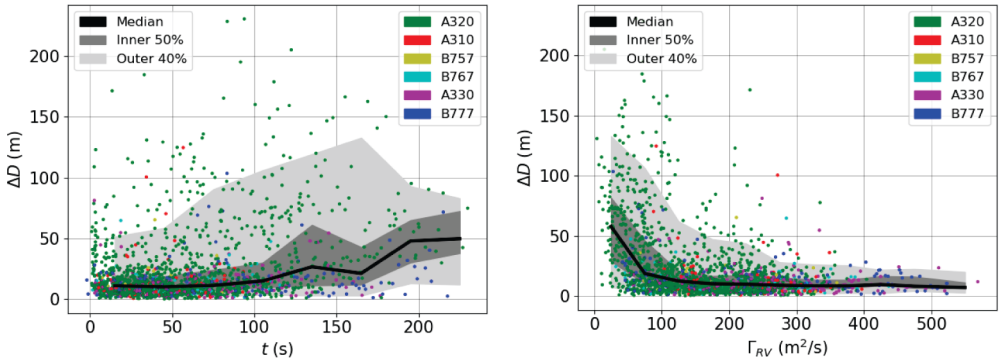

(a) Temporal evolution. (b) Circulation strength influence.

Fig. 15. CNN ΔD correlation to vortex parameters for plate down LiDAR scans.

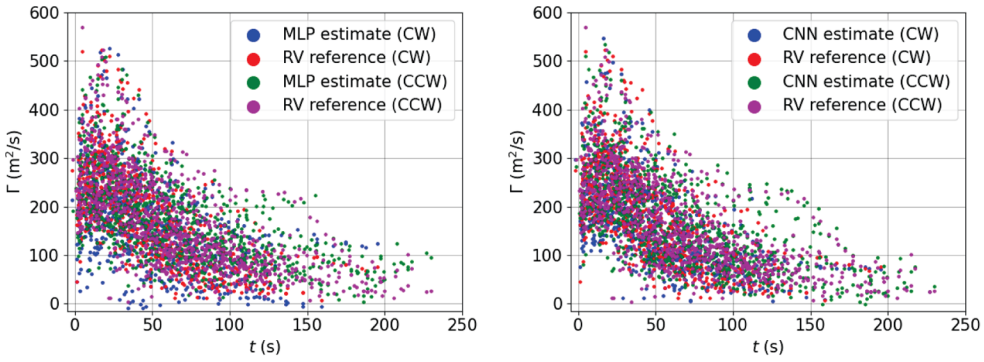

(a) MLPs. (b) CNNs.

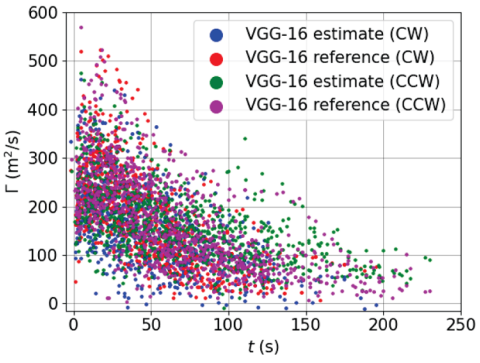

(c) VGG-16s.

Fig. 16. Temporal evolution of estimated vortex circulation without plates.

Optics EXPRESS

As done for the localization, we substantiate the above observations with statistical metrics for the circulation strength. For this purpose, a threshold circulation strength of 100 m^2/s is defined, above which a vortex is regarded a potential hazard to follower aircraft – regardless of its position above the runway. With analogous metric descriptions as for the localization metrics, the results in Table 6 confirm that CNNs are more reliable than MLPs also with respect to the hazard detection using vortex strengths. In particular the positive predictive rate promises satisfying hazard detection results using the CNNs, for both plate states.

Table 6. Statistics regarding the circulation characterization (CW and CCW vortices). Positive/negative are vortices above/below 100 m^2/s (gray = the superior network per plates state). The RV method is used for comparison.

Circulation metric	Plates down		Plates up	
	MLP	CNN	MLP	CNN
False-Positives rate (%)	35.2	17.6	42.9	19.9
False-Negatives rate (%)	8.8	7.4	14.4	9.6
Positive predictive rate (%)	87.3	93.3	85.6	93.1

The following provides further analysis on the results of the CNNs with respect to vortex age and vortex circulations of the RV method. Figure 17 introduces the relative vortex circulation error and the normalized vortex circulation error dependent on both vortex age (on top) and circulation strength (at the bottom). Both errors use the absolute difference between the circulation strength estimated by the RV method and the CNN i.e. $\Delta\Gamma = \mid \Gamma_{RV} - \Gamma_{CNN} \mid$. The relative circulation error is divided by the RV method's circulation to obtain $\Delta\Gamma/\Gamma_{RV}$. Similarly, the normalized circulation error $\Delta\Gamma^* = \Delta\Gamma/\Gamma_0$ is given by dividing the circulation error $\Delta\Gamma$ by the initial vortex circulation Γ_0 derived from the aircraft's maximum landing weight, air density and true airspeed as detailed in [16] (in rare cases Γ_0 is unavailable from this method, as an alternative mean values of that aircraft type are used - standard deviations of at most 4% promise to give representative Γ_0 values).

The expected trend of higher errors for older vortices (Fig. 17(a)) corresponding to lower circulation strengths (Fig. 17(c)) can be seen using the relative circulation error. The identified circulation threshold of about 100 m^2/s, until which CNN characterizations are precise and reliable is also confirmed with Fig. 17(c). From Fig. 17(b) and Fig. 17(d) one can conclude that smaller aircraft generating smaller and weaker vortices such as the A320, although forming a much larger part of the data set, are more difficult to characterize for the CNNs than larger aircraft such as the B777, even at the same vortex age or the same circulation strength.

6.1.3. Physical interpretability

One of the open research questions formulated in Section 2.3 focused on how results from ANNs for flow applications can be explained and trusted. In the field of ANNs this matter is named explainability. The lack of interpretability of ANN results is the most common critique when suggested for scientific purposes. As a consequence, the ANN community has been eager to develop methods that would allow comprehension of the ANN thinking process, ideally with capabilities to back-track ANN data flow and understanding what patterns the ANN has learned. The extent to which ANNs can be explained strongly depends on their type, for instance MLPs are far more complex to interpret than CNNs – another advantage of the latter ANN type. Below introduces one visualization technique: Grad-CAM [60] for wake vortex detection from LiDAR scans, with the purpose of showcasing that CNNs do not have to be black boxes.

Consider the exemplary LiDAR scan in Fig. 18(a), an input for which one of the many filters of the CNN maximizes its activation (Fig. 18(b)), the corresponding activation map for that

Optics EXPRESS

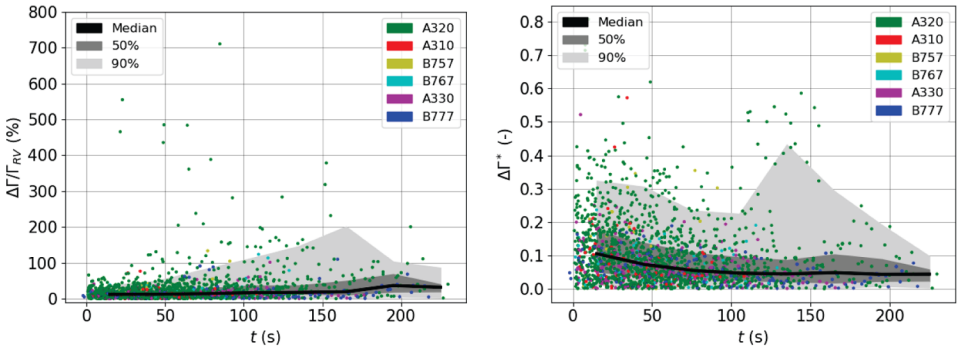

(a) Relative vortex circulation error against vortex age.

(b) Normalized vortex circulation error against vortex age.

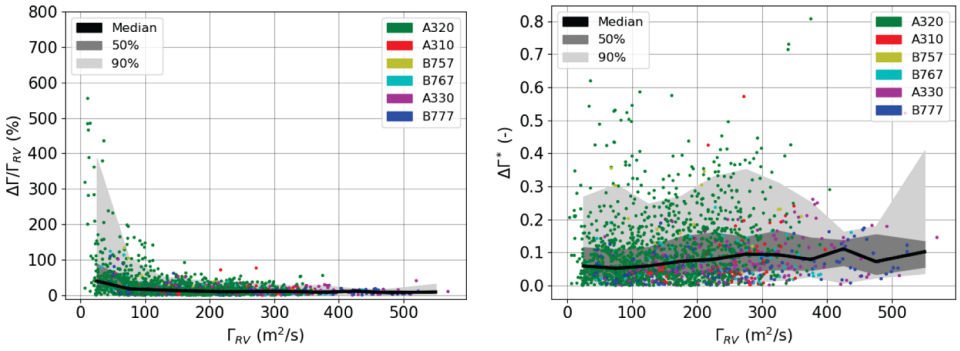

(c) Relative vortex circulation error against RV circulation strength.

(d) Normalized vortex circulation error against RV circulation strength.

Fig. 17. Circulation error dependent on vortex age and RV reference circulation without plates.

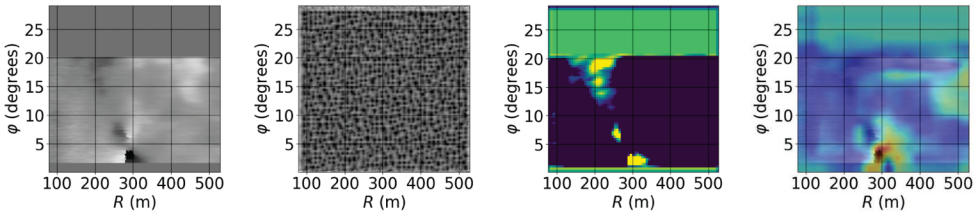

(a) Input LiDAR scan seen by the CNN (dark/bright are high/low radial velocities).

(b) Input for which an exemplary filter maximizes its activation (dark/bright are high/low radial velocities).

(c) Intermediate activation of the filter from the CNN (yellow represents high activations).

(d) Decision making activation CNN (warm colors mark recognized features).

Fig. 18. CNN visualizations for the CCW vortex elevation angle model.

Optics EXPRESS

filter (Fig. 18(c)), and the decision making activation for the CCW vortex elevation angle model (Fig. 18(d)). Figure 18(b), the idealized input scan to perfectly activate an exemplary filter (as it corresponds exactly to the pattern sought by the filter), illustrates how the filter searches for patches of high radial velocity as typically seen in wake vortex LiDAR scans. Besides some noise in the vicinity of R = 250 m and φ = 15° to 20°, the resulting activation map from this filter (Fig. 18(c)) highlights exactly these high radial velocity patches belonging to the vortex pair as seen in the LiDAR scan (Fig. 18(a)): the high radial velocity patch of the CW vortex is highlighted at R = 250 m and φ = 5° to 10°, and high radial velocity patch of the CCW vortex is highlighted at R = 300 m and φ = 0° to 5°. The final decision making heatmap (Fig. 18(d)) shows the model's capability to differentiate between the two vortices and also that not the high radial velocity patch is searched for, but the center of the vortex. For a CCW vortex, this is above the high positive radial velocities patch in Fig. 18(c), just as highlighted by the CNN in red color.

6.1.4. Computing times

While the majority of this paper has the aim to analyze whether ANNs are a potential alternative for wake vortex characterization in LiDAR scans, a concrete goal is to accelerate the processing speed of the evaluation in comparison to the currently used RV method. The RV method is not yet fully automated and on top has a processing period of several seconds for a single LiDAR scan. This work found that both MLPs and CNNs are considerably faster. Even with rather low-level hardware the characterization of a single LiDAR scan with MLPs takes around 0.10 s and CNNs take marginally longer, 0.16 s. Even though MLPs are quicker, this advantage can not justify characterizations with inferior precision and lower reliability. For all 100 epochs the training time of the ANNs (with the same hardware) takes 35 min and 810 min for the MLPs and CNNs, respectively. Data set sizes have a major impact on these durations, however since training is performed only once it has little relevance for the efficient operation of a WVAS.

6.2. Comparison to the modified VGG-16 ANNs

The custom CNNs are compared to the performance of the modified VGG-16 ANNs in order to assess whether custom ANN architectures can also deliver high performance LiDAR measurement processing results. Table 7 indicates that the modified VGG-16 ANNs are also capable of characterizing wake vortex data. However, the custom CNNs clearly outperform these certain VGG-16 ANNs in every category based on the LiDAR measurements without plates. Figure 12 and Fig. 16 have also already shown that the custom CNNs feature a higher reliability due to a lower spread in ΔD with vortex age and less False-Negatives (spurious low circulation values at young vortex ages), respectively.

Table 7. Validation errors comparing VGG-16 ANNs and CNNs with 8925 train and 700–1100 validate scans without plates (gray = lowest error per parameter).

ANN	Γ MAE (m^2/s)		φ_V MAE (°)		R_V MAE (m)		Mean/median ΔD (m)	
	CW	CCW	CW	CCW	CW	CCW	CW	CCW
CNN	32.24	25.76	1.40	1.00	21.51	20.51	22.70/11.49	21.89/12.39
VGG-16	58.81	51.86	2.04	1.49	48.75	35.09	49.84/39.09	36.91/27.58

It may be argued that the architecture of the VGG-16 ANN is too deep for wake vortex LiDAR scans, hence patterns found are too specific to the training data set and the ANN cannot generalize well to other data sets – the VGG-16 ANNs overfit. However, the inferior performance using VGG-16 ANNs may also be a result from other sources than the architecture. The bottom layers of the VGG-16 network, with pre-trained weights, were not trained with images that contain features similar to vortices. In fact, the ImageNet challenge contains pictures of everyday objects rather than aerodynamic phenomena. Hence, boundaries in the ImageNet images are potentially

Optics EXPRESS

more defined, or other disparities may exist to the wake vortex LiDAR scans. Nevertheless, the approach of this paper, to generate custom ANN architectures, allows understanding the effect of hyperparameters and the potential of the data set much more rigorously. On top of this, the training of a VGG-16 ANN with the previously outlined hardware takes nearly 39 h and evaluation of a single LiDAR scan requires around 145 s – an unacceptable processing speed.

6.3. Comparison to the state of the art LiDAR processing algorithms

Throughout this paper it has been stressed that one may not expect the herein presented ANN method might outperform current processing algorithms such as the RV method [28], in terms of accuracy. However, as we have seen in Section 6.1.4 it is two orders of magnitude faster. Targets for the CNNs originate from the RV method, which makes it conceptually impossible for the CNN characterizations to achieve a higher precision than those of the RV method. Nonetheless, a comparison of the performance between the state of the art algorithms and the custom CNNs appears useful. The characterization accuracies of the VE method [31] and RV method are described in Section 2.2, however it must be emphasized that the RV method accuracy is only an estimate for low turbulence scenarios based on two-dimensional simulated data and comparisons based on real data are a matter of future studies.

Table 8 confirms and quantifies the expected deficiency of the custom CNNs in comparison to the state of the art algorithms using the RMSEs and ΔD. The CNN performance without plates achieves a vortex strength characterization accuracy which is 2.5–3.5 times worse than the VE method, whereas the localization is about 1.5 times worse (focusing on the median ΔD and unifying the VE method errors). With plates the CNNs feature even higher errors.

Table 8. Validation errors comparing CNNs with state of the art algorithms.

ANN	Γ RMSE (m^2/s)		φ_V RMSE (°)		R_V RMSE (m)		Median ΔD (m)	
	CW	CCW	CW	CCW	CW	CCW	CW	CCW
CNN (no plates)	44.03	35.61	2.46	1.53	35.82	35.22	11.49	12.39
CNN (plates)	45.93	43.18	2.04	1.21	56.73	66.33	39.50	31.60
CNN (proxy)	8.15	6.78	0.27	0.37	2.93	2.80	1.71	0.76
RV method [28]	10.30		0.21		1.80		-	
VE method [32]	13.00		-		-		7.91	

On top of the limiting nature of the targets, the ANN operation itself introduces an error which can be modeled with the proxy data originally used for the design of the ANN architectures. Row three in Table 8 puts the ANN operation error into perspective using the artificial proxy data. As these proxy scans are free of noise or atmospheric turbulence, errors using real LiDAR measurement data will always be larger. The dependencies between the errors from the targets and the errors from the ANN procedure is unknown, however it is clear that when they are superimposed they build precision limits which the CNNs trained on the real LiDAR scans cannot surpass. Moreover, with the proxy data achieving accuracies in the same order of magnitude as the RV method, it appears unlikely that the current architectures could achieve real data accuracies close to the RV method. Overall, there is room for improvement with the proposed method, but the precision cannot outperform the stated precision of the RV method unless the targets are created in an independent manner, such as for example with high fidelity three-dimensional numerical landing simulations. Note that LiDAR instruments themselves bring about their intrinsic limitations - so it remains questionable whether precision beyond the RV method is possible in principle. The clear advantage of ANNs over the VE and RV methods, is their swift and automatic micro-PCDL scan processing. The presented achievable accuracy

Optics EXPRESS

estimates also provide a baseline for future investigations that employ ANNs for the wake vortex characterization.

7. Conclusion

The suitability of Artificial Neural Networks (ANNs) for the quantitative fast-time characterization of wake vortex circulation strength and position from Light Detection and Ranging (LiDAR) measurement data collected at Vienna International Airport has been investigated and evaluated. In contrast to preceding literature, the herein trained ANNs do not only detect wake vortices in LiDAR scans, but they also characterize the vortex parameters with an acceptable accuracy. When comparing these ANNs to the state of the art LiDAR processing algorithms, which lack full automation, significantly shorter evaluation times are made accessible via the ANNs. Artificial proxy data have been employed to accelerate ANN architecture development.

Application relevant pre-processing facilitates the characterization of wake vortices with ANNs. That is, using a LiDAR scan before an overflight to remove background crosswinds, employing a universal elevation-range grid, using separate ANNs for cases with and without plate lines installed to accelerate wake vortex decay, and disregarding measurements close to the ground. The custom designed Convolutional Neural Networks outperform both Multilayer Perceptrons as well as a readily available pre-trained modified version of the popular VGG-16 ANNs in the estimation of key parameters – the wake vortex center locations and circulation strengths. By utilizing custom ANN architectures, trade-offs between different pre-processing approaches and normalizations could be assessed, enabling better decision making. ANN processing speeds of up to 0.1 s for a single LiDAR scan and, depending on the potential hazard definition, a reliability of up to 93% suggest that rapid monitoring of fast-time wake vortex predictions as part of a wake vortex advisory system comes within reach. Additionally, the accuracy and ability to process large data sets as those collected at the Vienna airport could lead to ANN usage for other comprehensive measurement campaigns or routine measurements required for the introduction of temporal aircraft separations at individual airports.

The current paper investigated several methods for the wake vortex position and strength characterization based on LiDAR scans from landing aircraft using ANNs. It has been found that the suitability of ANNs for this task appears promising and that they should be investigated further to improve their performance while increasing their generalizability and possibly even surpassing the precision of current state of the art algorithms.

Funding. Deutsches Zentrum für Luft- und Raumfahrt (Wetter und disruptive Ereignisse); Horizon 2020 Framework Programme (731781).

Acknowledgments. The Vienna measurement campaign has received funding within the framework of the SESAR Joint Undertaking "Increased Runway and Airport Throughput" project (PJ.02 EARTH) within the European Union's Horizon 2020 research and innovation programme under grant agreement No 731781 as well as from the German Aerospace Research Center (DLR) project "Wetter und disruptive Ereignisse".

Disclosures. The authors declare no conflicts of interest.

Data availability. Data underlying the results presented in this paper are not publicly available at this time but may be obtained from the authors upon reasonable request.

References

1. J. N. Hallock and F. Holzäpfel, "A review of recent wake vortex research for increasing airport capacity," Progress in Aerospace Sciences **98**, 27–36 (2018).
2. A. Stephan, D. Rohlmann, F. Holzäpfel, and R. Rudnik, "Effects of detailed aircraft geometry on wake vortex dynamics during landing," J. Aircraft **56**(3), 974–989 (2019).
3. F. Rooseleer, V. Treve, R. Graham, and I. De Visscher, "Wake turbulence re-categorisation on approach and departure for safe and more efficient air traffic management," in *30th Congress of the International Council of the Aeronautical Sciences*, (ICAS, 2016), pp. 1–10.
4. F. Holzäpfel, T. Gerz, M. Frech, and A. Dörnbrack, "Wake vortices in convective boundary layer and their influence on following aircraft," J. Aircraft **37**(6), 1001–1007 (2000).

Optics EXPRESS

5. V. Rossow and K. James, "Overview of wake-vortex hazards during cruise," J. Aircraft **37**(6), 960–975 (2000).
6. J. Critchley and P. Foot, "Uk caa wake vortex database: analysis of incidents reported between 1982 and 1990," CAA Paper **91** (1991).
7. F. Holzäpfel and M. Steen, "Aircraft wake-vortex evolution in ground proximity: analysis and parameterization," AIAA J. **45**(1), 218–227 (2007).
8. T. Gerz, F. Holzäpfel, and D. Darracq, "Commercial aircraft wake vortices," Progress in Aerospace Sciences **38**(3), 181–208 (2002).
9. Eurocontrol, "Challenges of growth," Tech. rep., Eurocontrol (2018). European aviation in 2040.
10. J. Cheng, A. Hoff, J. Tittsworth, and W. A. Gallo, "The development of wake turbulence re-categoriza-tion in the united states," in *8th American Institute of Aeronautics and Astronautics Atmospheric and Space Environments Conference*, (2016), pp. 1–12.
11. F. Holzäpfel, "Probabilistic two-phase aircraft wake-vortex model: further development and assessment," J. Aircraft **43**(3), 700–708 (2006).
12. F. Holzäpfel, T. Gerz, M. Frech, A. Tafferner, F. Köpp, I. N. Smalikho, S. Rahm, K.-U. Hahn, and C. Schwarz, "The wake vortex prediction and monitoring system wsvbs part i: Design," Air Traffic Control Quarterly **17**(4), 301–322 (2009).
13. P. Weijun, D. Yingjie, Z. Qiang, T. Jiahao, and Z. Jun, "Deep learning for aircraft wake vortex identification," in *IOP Conference Series: Materials Science and Engineering*, vol. 685 (IOP Publishing, 2019), pp. 1–8.
14. P. Weijun, D. Yingjie, Z. Qiang, W. Zhengyuan, and L. Haochen, "Research on aircraft wake vortex recognition using alexnet," Opto-Electronic Eng. **46** (2019).
15. N. Baranov and B. Resnick, "Wake vortex detection by convolutional neural networks," European Journal of Electrical Engineering and Computer Science (EEACS) **3**, 92–97 (2021).
16. F. Holzäpfel, A. Stephan, G. Rotshteyn, S. Körner, N. Wildmann, L. Oswald, T. Gerz, G. Borek, A. Floh, C. Kern, M. Kerschbaum, R. Nossal, J. Schwarzenbacher, M. Strobel, L. Strauss, C. Weiß, S. Kauczok, C. Schiefer, H. Czekala, G. Maschwitz, and I. Smalikho, "Mitigating wake turbulence risk during final approach via plate lines," AIAA J. **59**(11), 4626–4641 (2021).
17. N. Wartha, A. Stephan, F. N. Holzäpfel, and G. Rotshteyn, "Characterizing wake vortices of landing aircraft using artificial neural networks and lidar measurements," in *AIAA AVIATION 2021 FORUM*, (2021), pp. 1–19.
18. R. E. Robins, D. P. Delisi, and G. C. Greene, "Algorithm for prediction of trailing vortex evolution," J. Aircraft **38**(5), 911–917 (2001).
19. J. Harvey and F. J. Perry, "Flowfield produced by trailing vortices in the vicinity of the ground," AIAA J. **9**(8), 1659–1660 (1971).
20. P. Spalart, M. K. Strelets, A. Travin, and M. Shur, "Modeling the interaction of a vortex pair with the ground," Fluid Dynamics **36**(6), 899–908 (2001).
21. Z. Zheng and R. L. Ash, "Study of aircraft wake vortex behavior near the ground," AIAA J. **34**(3), 580–589 (1996).
22. A. Stephan, F. Holzäpfel, and T. Misaka, "Aircraft wake-vortex decay in ground proximity–physical mechanisms and artificial enhancement," J. Aircraft **50**(4), 1250–1260 (2013).
23. F. Köpp, "Doppler lidar investigation of wake vortex transport between closely spaced parallel runways," AIAA J. **32**(4), 805–810 (1994).
24. A. Stephan, F. Holzäpfel, and T. Misaka, "Hybrid simulation of wake-vortex evolution during landing on flat terrain and with plate line," Int. J. Heat and Fluid Flow **49**, 18–27 (2014).
25. F. Bao and H. Vollmers, "Alleviation of end-effect in facilities for far wake investigations," in *43rd AIAA Aerospace Sciences Meeting and Exhibit*, (2005), p. 907.
26. H. Moet, F. Laporte, G. Chevalier, and T. Poinsot, "Wave propagation in vortices and vortex bursting," Phys. Fluids **17**(5), 054109 (2005).
27. A. Stephan, F. Holzäpfel, T. Misaka, R. Geisler, and R. Konrath, "Enhancement of aircraft wake vortex decay in ground proximity," CEAS Aeronaut. J. **5**(2), 109–125 (2014).
28. I. N. Smalikho, V. Banakh, F. Holzäpfel, and S. Rahm, "Method of radial velocities for the estimation of aircraft wake vortex parameters from data measured by coherent doppler lidar," Opt. Express **23**(19), A1194–A1207 (2015).
29. I. N. Smalikho and V. Banakh, "Estimation of aircraft wake vortex parameters from data measured with a 1.5-μ m coherent doppler lidar," Opt. Lett. **40**(14), 3408–3411 (2015).
30. F. Köpp, S. Rahm, and I. N. Smalikho, "Characterization of aircraft wake vortices by 2-μ m pulsed doppler lidar," J. Atmos. Oceanic Technol. **21**(2), 194–206 (2004).
31. V. Banakh and I. N. Smalikho, *Coherent Doppler Wind Lidars in a Turbulent Atmosphere* (Artech House, 2013), chap. 5.
32. F. Köpp, S. Rahm, I. N. Smalikho, A. Dolfi, J.-P. Cariou, M. Harris, and R. I. Young, "Comparison of wake-vortex parameters measured by pulsed and continuous-wave lidars," J. Aircraft **42**(4), 916–923 (2005).
33. M. J. Pruis, D. P. Delisi, D. Jacob, and D. Y. Lai, "Summary of nasa wake and weather data collection at memphis international airport: 2013-2015," in *8th AIAA Atmospheric and Space Environments Conference*, (2016), p. 3274.
34. P. Weijun, Z. Wu, and X. Zhang, "Identification of aircraft wake vortex based on svm," Math. Probl. Eng. **2020** (2020).

Optics EXPRESS

35. C.-F. Teng, C.-C. Liao, C.-H. Chen, and A.-Y. A. Wu, "Polar feature based deep architectures for automatic modulation classification considering channel fading," in *2018 IEEE Global Conference on Signal and Information Processing (GlobalSIP)*, (IEEE, 2018), pp. 554–558.
36. J. Redmon, S. Divvala, R. Girshick, and A. Farhadi, "You only look once: Unified, real-time object detection," in *Proceedings of the IEEE conference on computer vision and pattern recognition*, (2016), pp. 779–788.
37. A. Toshev and C. Szegedy, "Deeppose: Human pose estimation via deep neural networks," in *Proceedings of the IEEE conference on computer vision and pattern recognition*, (2014), pp. 1653–1660.
38. J. Ribera, D. Guera, Y. Chen, and E. J. Delp, "Locating objects without bounding boxes," in *Proceedings of the IEEE Conference on Computer Vision and Pattern Recognition*, (2019), pp. 6479–6489.
39. J. J. Tompson, A. Jain, Y. LeCun, and C. Bregler, "Joint training of a convolutional network and a graphical model for human pose estimation," in *Advances in Neural Information Processing Systems 27*, vol. 27 Z. Ghahramani, M. Welling, C. Cortes, N. D. Lawrence, and K. Q. Weinberger, eds. (Curran Associates, Inc., 2014), pp. 1799–1807.
40. Y. Sun, X. Wang, and X. Tang, "Deep convolutional network cascade for facial point detection," in *Proceedings of the IEEE conference on computer vision and pattern recognition*, (2013), pp. 3476–3483.
41. B. Shi, X. Bai, W. Liu, and J. Wang, "Face alignment with deep regression," IEEE Trans. Neural Netw. Learning Syst. **29**(1), 183–194 (2018).
42. J. Deng, W. Dong, R. Socher, L.-J. Li, K. Li, and L. Fei-Fei, "Imagenet: A large-scale hierarchical image database," in *2009 IEEE conference on computer vision and pattern recognition*, (IEEE, 2009), pp. 248–255.
43. K. Simonyan and A. Zisserman, "Very deep convolutional networks for large-scale image recognition," arXiv preprint arXiv:1409.1556 (2014).
44. F. Chollet, "Keras," https://keras.io (2015).
45. N. N. Ahmad and F. Proctor, "Review of idealized aircraft wake vortex models," in *52nd Aerospace Sciences Meeting*, (2014), pp. 1–28.
46. H. Lamb, *Hydrodynamics* (Dover, 1923), 6th ed.
47. S. L. Brunton, B. R. Noack, and P. Koumoutsakos, "Machine learning for fluid mechanics," Annu. Rev. Fluid Mech. **52**, 477–508 (2020).
48. S. S. Cross, R. F. Harrison, and R. L. Kennedy, "Introduction to neural networks," The Lancet **346**(8982), 1075–1079 (1995).
49. F. Chollet, *Deep Learning with Python* (Manning Publications Company, 2017), chap. 2–5.
50. A. Krizhevsky, I. Sutskever, and G. E. Hinton, "Imagenet classification with deep convolutional neural networks," in *Advances in neural information processing systems*, (2012), pp. 1097–1105.
51. B. Colvert, M. Alsalman, and E. Kanso, "Classifying vortex wakes using neural networks," Bioinspiration & biomimetics **13** (2018).
52. K. O'Shea and R. Nash, "An introduction to convolutional neural networks," arXiv preprint arXiv:1-511.08458 (2015).
53. A. Géron, *Hands-On Machine Learning with Scikit-Learn, Keras, and TensorFlow - Concepts, Tools, and Techniques to Build Intelligent Systems* ("O'Reilly Media, Inc.", 2019), chap. 10, 2nd ed.
54. I. Arel, D. C. Rose, and T. P. Karnowski, "Deep machine learning - a new frontier in artificial intelligence research - research frontier," IEEE Comput. Intell. Mag. **5**(4), 13–18 (2010).
55. W. Hou, D. Darakananda, and J. D. Eldredge, "Machine-learning-based detection of aerodynamic disturbances using surface pressure measurements," AIAA J. **57**(12), 5079–5093 (2019).
56. D. P. Kingma and J. Ba, "Adam: A method for stochastic optimization," arXiv preprint arXiv:1412.-6980 (2014).
57. R. Jiang and S. Mei, "Polar coordinate convolutional neural network: From rotation-invariance to translation-invariance," in *2019 IEEE International Conference on Image Processing (ICIP)*, (IEEE, 2019), pp. 355–359.
58. T. Gurke and H. Lafferton, "The development of the wake vortices warning system for frankfurt airport: Theory and implementation," Air Traffic Control Quarterly **5**(1), 3–29 (1997).
59. F. Holzäpfel, T. Gerz, F. Köpp, E. Stumpf, M. Harris, R. I. Young, and A. Dolfi-Bouteyre, "Strategies for circulation evaluation of aircraft wake vortices measured by lidar," J. Atmos. Oceanic Technol. **20**(8), 1183–1195 (2003).
60. R. R. Selvaraju, M. Cogswell, A. Das, R. Vedantam, D. Parikh, and D. Batra, "Grad-cam: Visual explanations from deep networks via gradient-based localization," in *Proceedings of the IEEE international conference on computer vision*, (2017), pp. 618–626.